APPLIED PHYSICS

Nanostructure, osteopontin, and mechanical properties of calcitic avian eggshell

Dimitra Athanasiadou,[1] Wenge Jiang,[1] Dina Goldbaum,[2] Aroba Saleem,[2] Kaustuv Basu,[3] Michael S. Pacella,[4]* Corinna F. Böhm,[5] Richard R. Chromik,[2] Maxwell T. Hincke,[6] Alejandro B. Rodríguez-Navarro,[7] Hojatollah Vali,[3,8] Stephan E. Wolf,[5,9] Jeffrey J. Gray,[10,11] Khanh Huy Bui,[8] Marc D. McKee[1,8]†

Avian (and formerly dinosaur) eggshells form a hard, protective biomineralized chamber for embryonic growth—an evolutionary strategy that has existed for hundreds of millions of years. We show in the calcitic chicken eggshell how the mineral and organic phases organize hierarchically across different length scales and how variation in nanostructure across the shell thickness modifies its hardness, elastic modulus, and dissolution properties. We also show that the nanostructure changes during egg incubation, weakening the shell for chick hatching. Nanostructure and increased hardness were reproduced in synthetic calcite crystals grown in the presence of the prominent eggshell protein osteopontin. These results demonstrate the contribution of nanostructure to avian eggshell formation, mechanical properties, and dissolution.

INTRODUCTION

The avian (and formerly dinosaur) eggshell is a thin, mineralized (calcite) layer that adequately protects the egg content and allows for the extra-uterine development of the chick embryo. Besides its protective function, its partial dissolution and thinning from the inside out during fertilized egg incubation serve as a source of calcium required for calcium-phosphate mineralization of the growing embryonic chick skeleton. This partial dissolution of the inner aspect of the shell also facilitates chick hatching/pipping. We hypothesized that these diverse functions of the remarkably designed and evolutionarily persistent avian eggshell likely result from regional differences in nanostructure; basic eggshell structure has been conserved over hundreds of millions of years of evolution.

The eggshell of the domestic chicken (*Gallus gallus*) is about 95% (by weight) calcium-carbonate mineral in the form of calcite and about 3.5% (by weight) organic material/matrix (including water) (*1*). Among hundreds of proteins identified by proteomics and various other means in the eggshell organic matrix (*2*–*5*), osteopontin (OPN, the name derived from its initial discovery in bone) is a major shell matrix protein (*6*) and a member of a group of mineral-binding proteins (*7*) thought to be prominent in guiding mineralization processes because of their particularly high negative charge and open flexible structure (*7*, *8*). These proteins are intrinsically disordered (*8*) and are thought to have arisen from ancestral gene-duplication events. Their high negative charge (involved in calcium binding and mineral binding) partly derives from an abundance of acidic amino acids (Asp and Glu). In addition, many Ser residues are phosphorylated (this is particularly so for OPN), which imparts additional negative charge to bind ionic calcium and crystal lattice calcium (*9*).

Living organisms produce a wide variety of biominerals for a variety of purposes. Biominerals form hardened structures that often have complex architectures that are hierarchically organized, such as the human skeleton where calcium-phosphate mineral prevails, with nanocrystals forming within an extensive, fibrillar organic macromolecular assembly known as the extracellular matrix. On the other hand, terrestrial and marine organisms typically use calcium-carbonate mineral polymorphs to build functionalized biomineralized structures such as seashells, snail shells, and eggshells. These rigid structures are hybrid composite materials where organic-inorganic (protein-mineral) interactions largely improve mechanical properties, such as hardness and toughness, to adequately provide supportive and/or protective functions to the organism in which they are assembled (*10*).

In recent years, there has been much work focusing on the structural analysis of various calcareous biominerals at the nanometer length scale. In many cases, closely packed nanosized subunits that are essentially perfectly aligned have been observed to form through nonclassical crystallization pathways (*11*). These alternative pathways may give rise to crystalline material having a nanogranular structure that produces a single-crystal diffraction pattern as would be obtained for a single, "monolithic" crystal otherwise not having a nanosubstructure. Mollusk shells, fish otoliths, coral skeletons, and brachiopods all have been described as having an internal nanogranular structure (*12*). Although in vitro experiments have evaluated the influence of organic material on calcium-carbonate polymorph selection (*13*), little is actually known about the mechanisms through which biomolecules affect nanogranular structure in living organisms.

Here, we have investigated, at the nanoscale, the structure of the eggshell from chicken (*G. gallus*) and OPN incorporation and have identified the existence of nanogranular structure in this shell. We have additionally correlated this nanostructure with functional properties (hardness, elastic modulus, and dissolution). These findings extend our knowledge of how incorporated organic constituents can substantially enhance mechanical properties and controlled solubility in biostructures

---

[1]Faculty of Dentistry, McGill University, Montreal, Quebec H3A 0C7, Canada. [2]Department of Mining and Materials Engineering, McGill University, Montreal, Quebec H3A 0C5, Canada. [3]Facility for Electron Microscopy Research, McGill University, Montreal, Quebec H3A 0C7, Canada. [4]Department of Biomedical Engineering, Johns Hopkins University, Baltimore, MD 21218, USA. [5]Department of Materials Science and Engineering, Institute of Glass and Ceramics, Friedrich-Alexander-University Erlangen-Nürnberg, Erlangen 91058, Germany. [6]Department of Cellular and Molecular Medicine and Department of Innovation in Medical Education, University of Ottawa, Ottawa, Ontario K1H 8M5, Canada. [7]Departamento de Mineralogía y Petrología, Universidad de Granada, Granada 18002, Spain. [8]Department of Anatomy and Cell Biology, McGill University, Montreal, Quebec H3A 0C7, Canada. [9]Interdisciplinary Center for Functional Particle Systems, Friedrich-Alexander University Erlangen-Nürnberg, Haberstrasse 9a, Erlangen 91058, Germany. [10]Department of Chemical and Biomolecular Engineering, Johns Hopkins University, Baltimore, MD 21218, USA. [11]Program in Molecular Biophysics, Institute for Nanobiotechnology, Sidney Kimmel Comprehensive Cancer Center, Johns Hopkins University, Baltimore, MD 21218, USA.
*Present address: Department of Chemical and Biomolecular Engineering, Johns Hopkins University, Baltimore, MD 21218, USA.
†Corresponding author. Email: marc.mckee@mcgill.ca

(*14*), observations that align with alloy fabrication studies showing that dual-phase nanostructuring can nearly attain theoretical ("ideal") strength in synthesized materials (*15*). Here, we correlate nanostructure with hardness and elastic modulus in the chicken eggshell. We also describe changes in shells from eggs that have been partially naturally dissolved after physiologic fertilization and incubation, two processes required for chick embryo development. Finally, we report that occluded OPN (an abundant protein in eggshell) can induce nanostructure in synthetic (nonbiogenic) calcite, much like what we have observed in the chicken eggshell.

RESULTS AND DISCUSSION

Nanostructure of avian eggshell (chicken, *G. gallus)*

Here, systematic atomic force microscopy (AFM) analysis of each eggshell region [shown broadly for orientation purposes at low magnification by scanning electron microscopy (SEM) in Fig. 1A] revealed that the outermost vertical crystal layer (VCL), the central palisades layer (PL), and the innermost mammillary layer (ML) all have a fine nanostructure varying in size depending on the layer in which it was observed (Fig. 1, B to F). Topographic imaging by AFM operated in the amplitude mode demonstrated an average (±SD) nanostructure size

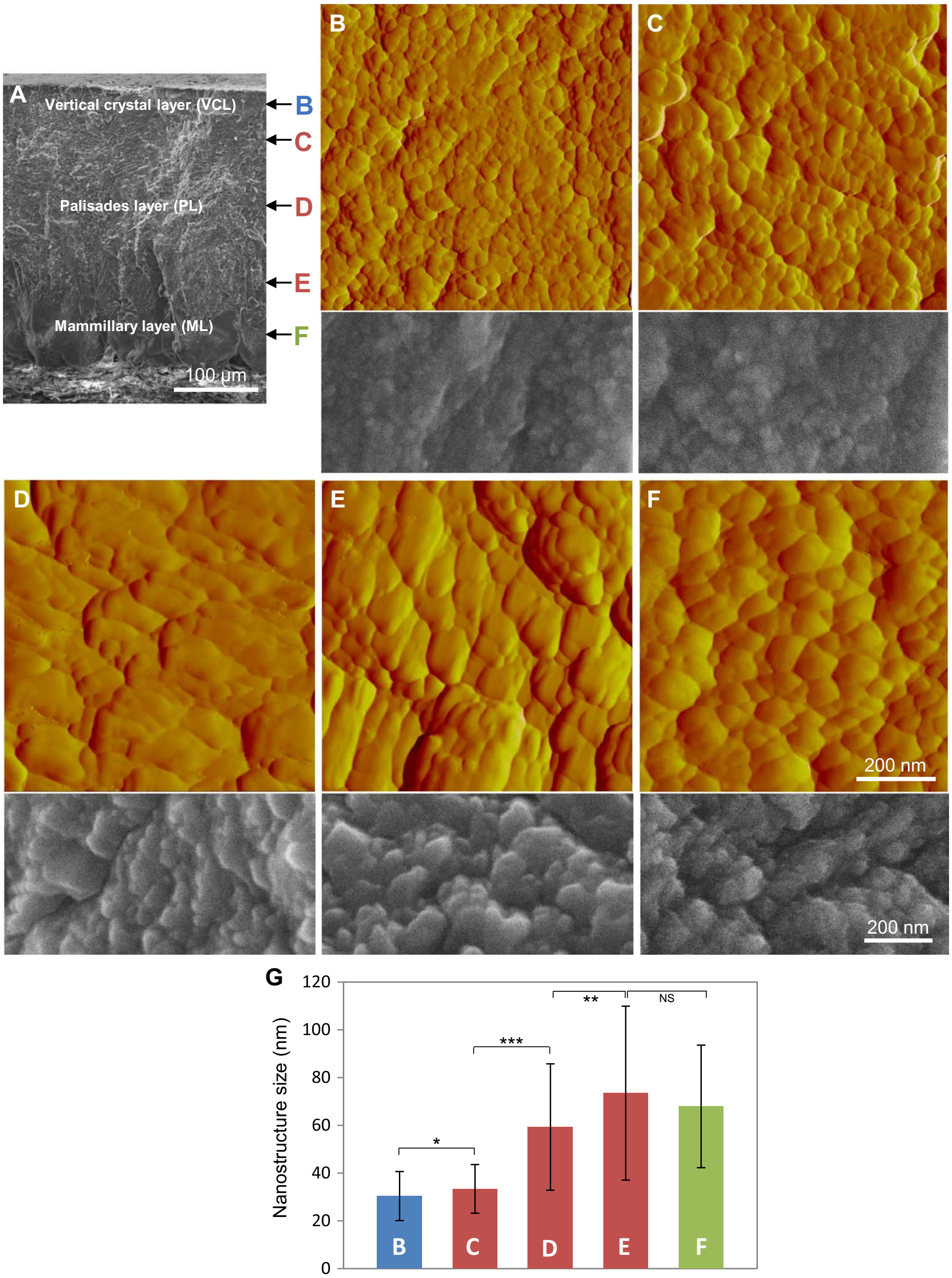

Fig. 1. The nanostructure of chicken eggshell (*G. gallus*). (**A**) SEM microstructure at low magnification and regional nomenclature of avian eggshell. (**B** to **F**) AFM (top; with a scanning area of 800 nm × 800 nm) and SEM (bottom) images of eggshell nanostructure as observed from the regions indicated in (A). (**G**) Histogram of nanostructure size distribution (Feret diameter) in the VCL (B), upper PL (C), middle PL (D), lower PL (E), and ML (F) layers. Significant difference is indicated by brackets (*$P < 0.05$, **$P < 0.01$, and ***$P < 0.001$). No significant difference (NS) ($P > 0.05$) between bars E and F. Values were compared by a two-tailed Student's *t* test.

(Feret diameter) of 30 ± 10 nm in the VCL, 33 ± 10 nm in the upper PL, 59 ± 27 nm in the middle PL, 74 ± 36 nm in the lower PL, and 68 ± 26 nm in the ML (Fig. 1G). Figure S1 shows the distribution of measured nanostructure size of the eggshell layers as determined from the AFM images from eggs that were not incubated and after 15 days of egg incubation. In addition, fig. S2 provides the average nanostructure area for all eggshell layers after 15 days of egg incubation. Changes in both nanostructure Feret diameter and area measurements were consistent in their variation between layers. SEM imaging performed on the same layers confirmed the variation in nanostructure size across the eggshell thickness (Fig. 1). Within the three sublayers of the PL that we sampled (upper, middle, and lower PL), average nanostructure size (by Feret diameter) continuously increased toward the interior of the shell in this layer, which is the region that forms the main bulk of the shell. In other bird species, previous AFM examination of all layers in the guinea fowl (*Numida meleagris*) and goose (*Anser anser*) eggshell showed a structuring described as "rounded nanogranules" (*16*)—such observations in these species are consistent with our findings in the chicken eggshell. In that previous study, nanogranular size was in the range of 50 to 100 nm, values close to the range of sizes that we have measured in the chicken shell layers and similar to those observed in other calcium-carbonate biominerals (*17*, *18*). More recently, Rodríguez-Navarro *et al.* (*19*) provided evidence for early nanogranular structuring at the first phase of chicken eggshell deposition where transient, flat, and disk-shaped amorphous calcium carbonate (ACC) forms on the eggshell membranes. However, there has been no detailed description of complete, intact, fully formed chicken eggshell at the nanoscale level to date.

Crystallographic features of the chicken eggshell include notable internal misalignments observed at the nanoscale in the columnar calcitic crystal units. These internal misalignments presumably occurred, at least in part, from the nonhomogeneous occlusion of abundant organic material (Fig. 2A). This was identified broadly by optical microscopy under cross-polarized light, where different degrees of light elimination occur from different microscale regions (Fig. 2B). This was further examined with greater resolution by electron backscatter diffraction (EBSD), where diffraction deviations within the calcitic columnar units (here pseudocolored, with deviations appearing as slight color shade differences) reflect the presence of substantial internal misalignments, generated at specific points and extending and propagating during calcite column growth (Fig. 2, C to E). Moreover, the 001 pole figure of a columnar calcite unit showed the orientation of *c*-axis deviations to be in the range of several degrees (up to 3° and even higher) (fig. S3A; whereas for a perfect single crystal, all the points in the pole figure would be concentrated in a single spot). EBSD data also show that there is an increase in internal misalignment with increasing column widths (fig. S3B), which implies that there is an accumulation of defects during eggshell calcitic column growth, further supporting the concept of a nanogranular crystal growth mechanism. Previous EBSD analysis of chicken eggshell and other eggshell species (*16*, *20*) has also shown that the PL consists of elongated, well crystallographically ordered single crystals of calcite; however, no evidence of internal misalignments of these elongated crystals was described. Thus, these internal misalignments were further investigated by two-dimensional x-ray diffraction (2D XRD). This confirms that the calcitic columnar units were not perfect

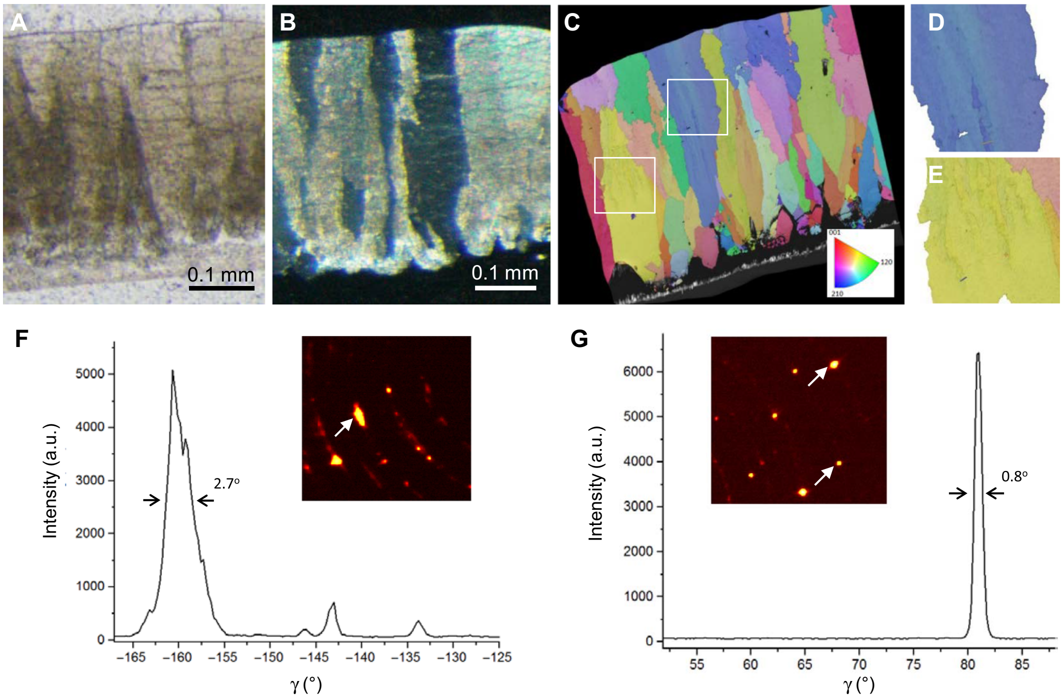

Fig. 2. Optical microscopy, EBSD, and 2D XRD of chicken eggshell. (**A**) Thin eggshell cross section viewed by conventional bright-field light microscopy showing nonhomogeneous distribution of organic and inorganic material throughout the eggshell layers. (**B**) Thin eggshell cross section [same as in (A)] viewed under cross-polarized light showing multiple, closely packed and well-defined columnar calcite units. (**C**) Crystal orientation map obtained by EBSD of a polished eggshell cross section showing slight internal crystalline misalignments (up to 4°) within the columns as depicted by different pseudocolor shades [see selected boxed areas in (**D**) and (**E**)]. (**F**) 2D XRD of a cross section of an eggshell showing an elongated single-crystal diffraction spot (arrows) and the associated intensity profile of a 104 calcite reflection as a function of the γ angle. Note the widening of the 104 peak due to varying crystallographic orientation within a columnar calcite unit. a.u., arbitrary units. (**G**) 2D XRD of a control powdered Iceland spar calcite crystal showing single-crystal diffraction spots (arrows) and the associated intensity profile of a 104 calcite reflection as a function of the γ angle.

single crystals but rather had a high degree of internal misorientations characterized by angular spreading of the diffraction spots (>2.5°) (Fig. 2F), producing elongated reflection spots (Fig. 2F, inset). In contrast, gently ground geologic calcite (Iceland spar)—commonly used as a reference, high-quality single-crystal control material for calcite—produced sharp, rounded spots (Fig. 2G, inset) with a much smaller angular spread (<0.8°) (Fig. 2G). To discard the possibility that these elongated spots were overlapping spots obtained from two or more columnar units, we recorded multiple 2D patterns after rotating the eggshell through 0.3° steps. Together, both the EBSD data and the 2D XRD data—which are complementary techniques—confirm the presence of deviating crystalline subdomains within the calcitic columnar units. These findings describing events occurring within the calcitic eggshell columns emphasize that nanostructure and slight alignment deviations result from a nonclassical crystal growth pathway (*11*).

Eggshell calcite crystals are known to form initially through the deposition of ACC particles that transform directly into calcite while preserving the granular nanostructure of the ACC (*19*). The newly crystallized material can adopt the orientation of previously formed calcite crystals (that is, in the ML) so that the crystallographic orientation is propagated as the columnar calcite crystal units develop by epitaxial nucleation (*21*). Amorphous nanoparticles responsible for the nanostructural morphology of many mineral formations in many organisms can occur as an initial precursor phase stabilized by resident organics, and these can be subsequently crystallized after contact with a crystalline substrate (*12*, *22*–*24*). In the eggshell, the interplay between organics and mineral precursors likely influences mineralization events leading to internal misalignments.

Given our AFM and SEM findings showing a gradient in nanostructure size across the thickness of the eggshell, we examined the structure of the PL in greater detail after using focused-ion beam (FIB) sectioning for further analysis by high-resolution transmission electron microscopy (HRTEM) and electron tomography. Bright-field TEM imaging (Fig. 3A) of the prepared FIB section revealed the presence of small mineral nanodomains ranging from 5 to 7 nm in diameter. Nanostructure is also evident at lower TEM magnifications, as shown by both bright-field (fig. S4A) and dark-field (fig. S4B) imaging. Higher-magnification lattice imaging by TEM revealed lattice fringes in these smaller nanodomains, indicating their crystalline nature (Fig. 3B). Selected-area electron diffraction (SAED) of these regions showed a coherent orientation of these smaller nanodomains (Fig. 3B, inset). Electron tomography of these areas provided 3D reconstructions of

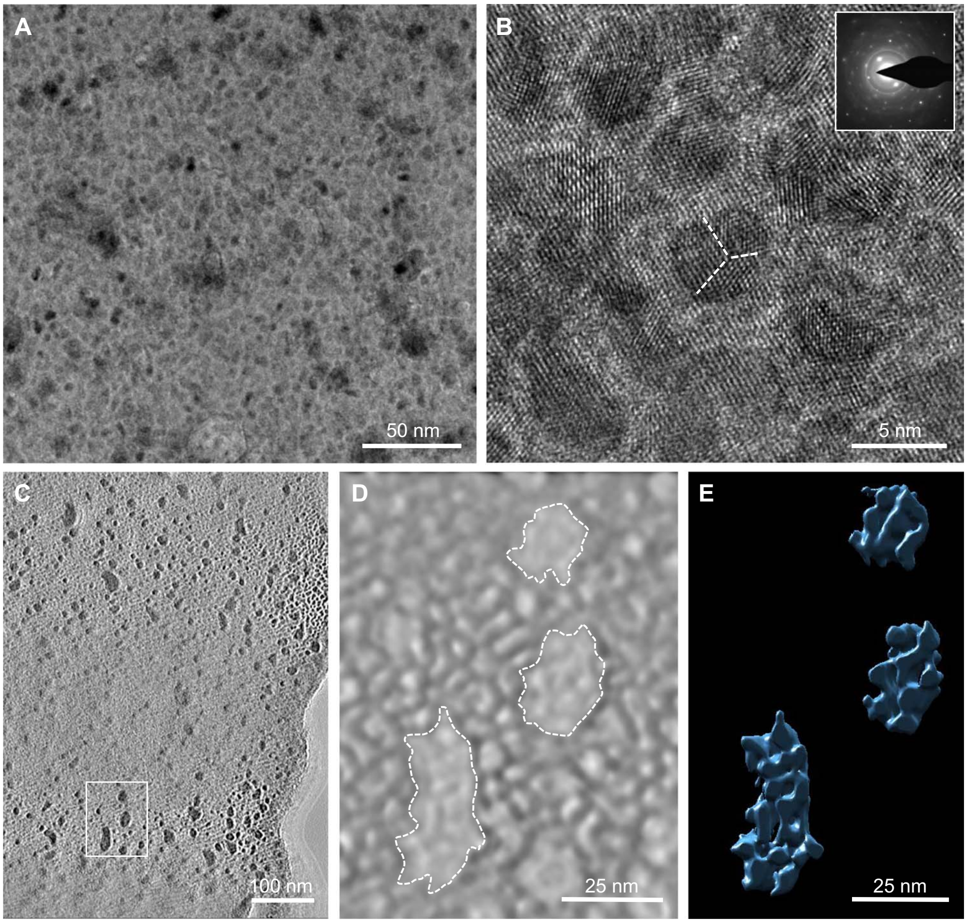

Fig. 3. Electron microscopy of a nanodomain substructure in the PL. (**A**) Bright-field unstained TEM image of chicken eggshell after FIB sectioning of the PL showing mineral nanodomains with a diameter of 5 to 7 nm. (**B**) HRTEM lattice imaging of the nanodomains, with SAED (inset) showing both a single-crystal diffraction spot pattern and polycrystalline-derived diffraction rings. Evidence for further mineral suborientations within the nanodomains is indicated by the dashed lines. Contrast differences in (A) and (B) presumably result from the relative distributions of a mixture of organic and inorganic (amorphous and crystalline) components. (**C**) Single bright-field TEM image from a tilt series of the nanodomains in the PL. (**D** and **E**) 3D tomographic reconstructions of the same nanodomain region indicated by a box in (C) [solid rendering in (D) and surface rendering in (E)]. The surface rendering in (E) used a threshold that shows only the high-density regions indicated by the dashed lines in (D).

this PL nanostructure (Fig. 2, C to E, and movies S1 and S2) where abundant and homogeneously dispersed 5- to 7-nm nanodomains were observed to reside within the larger nanostructure initially observed topographically by AFM and SEM (Fig. 1C). To confirm this observation using an alternative sample-preparation method, a wedge-polished section of the PL was prepared and thinned using a previously described method (*18*), and similar results were obtained (fig. S4C). Our work is consistent with observations by Lammie *et al.* (*25*) who used microfocused, small-angle x-ray scattering to report on "nanotexture" variations averaging ~4.5 nm in the PL, a feature that we believe we have now directly visualized and characterized in the present study. In the report of Lammie *et al.*, the nanotexture was attributed to voids presumably occupied by globular organic matrix, whereas here, we identify and visualize actual nanostructured, crystalline mineral in 2D and 3D that produces nanostructured texture (and we also present data on protein distribution; see below). Both sets of findings are consistent with the notion that regional variations in organic/protein content (*3*) [acting as activators or inhibitors of mineralization (*2*)], along with relative differences in the amounts, organization, and location of calcite and ACC, all likely contribute to producing the nanostructured texture (*19*).

In avian eggs, although the biological benefits of eggshell hierarchical structure (from the nanoscale to the macroscale) for the developing organism (chick) are apparent, the mechanism of nanostructure formation in the chemically crowded (organic and inorganic), and physically confined, milieu is less clear. As a possibility, the formation of pseudoperiodic structures of a uniform size can be explained by the reaction-diffusion model, which is also known as the Turing pattern (*26*). Turing patterns are abundant in nature and have remarkable significance in morphogenesis (*27*). The basis of the reaction-diffusion pattern formation is in the competition of two or more oscillating processes having different kinetic constants (for example, short-range activation and long-range inhibition) originating from local instabilities within an initially homogeneous steady-state system (*26*). In the laying hen, uterine fluid bathing the late developing egg (and then the eggshell) is supersaturated with respect to calcite and contains abundant calcium-binding proteins in a metastable system. In this system, heteronucleation events are likely to develop as local instabilities, where the competing processes are the Ca/P ion supply (activation) and the local ion depletion around the growing crystallites (inhibition). Notably, local ion depletion around a growing calcite crystal or a stabilized ACC particle has been demonstrated in the aqueous state in real time, and moreover, the extent of the depletion zone was proportional to mineral particle size (*28*). These reaction-diffusion kinetics could explain the formation of numerous small domains surrounded by a narrow depletion zone or fewer, larger, and more stable domains surrounded by a broader depletion zone, this possibly being a function of ion supply and OPN concentration (and/or other shell proteins) at different stages of eggshell formation (*29*).

OPN and the organic matrix compartment in chicken eggshell

In avian eggshell, OPN was first reported by Pines *et al.* (*6*) who detected strong OPN gene expression by cells specifically in the shell gland that was coincident with eggshell mineralization. In that previous work, immunohistochemistry and light microscopy were used to show that OPN was distributed throughout the shell. Since then, these findings on OPN and eggshell have been confirmed and developed by us and others using a variety of analytical methods (*2*, *30*, *31*). Here, Fig. 4A shows OPN retrieved biochemically from protein extracts of demineralized chicken eggshell. Figure 4B demonstrates OPN localization in situ in eggshell by immunohistochemistry at the light microscope level and ultrastructurally by immunogold labeling at the electron microscope level (Fig. 4C). Regional variations in the concentration of OPN are apparent [Fig. 4, B (brackets) and C (arrows)]; note that the demineralization procedure itself imparts substantial alterations to the localization pattern as the mineral dissolves and the organic matrix network partially collapses. Qualitatively, by immunostaining, OPN was most abundant in the VCL/PL and least abundant in the ML. Semiquantification of this immunolabeling using intensity-profile, linear plot views obtained from immunostained eggshell sections using ImageJ (fig. S5A) showed consistently high concentration of OPN in the outermost VCL layer, followed by a steady decline in OPN content toward the ML layer (fig. S5B). These results are in agreement with quantitative proteomics revealing that eggshell OPN levels are highest during development of the PL (*32*). Other proteomic data from eggshells obtained at various stages of formation, as retrieved from the shell gland of laying hens, have revealed an extensive protein incorporation profile at all stages of shell formation (*3*, *4*). Proteins (and other organics) that constitute the organic matrix of the shell interlace extensively, but variably, throughout all regions of the mineralized shell. How this cohabitation with calcium-carbonate mineral occurs remains poorly understood—a compartmental feature particularly surprising given the highly ordered (albeit with some misalignment) calcite mineral organization.

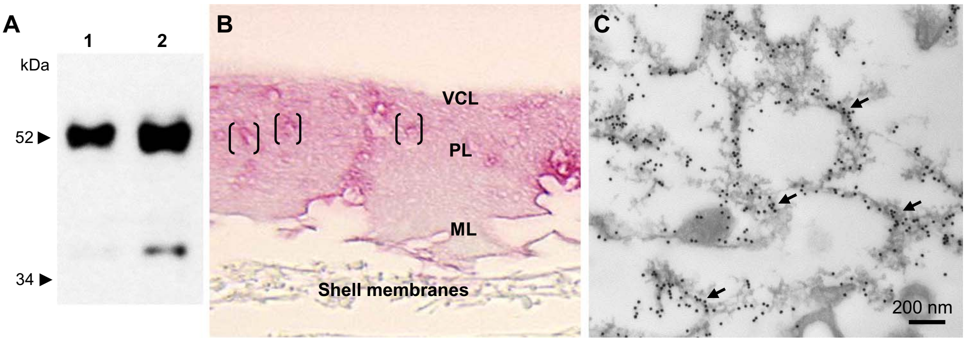

Fig. 4. OPN in chicken eggshell. (**A**) Immunoblotting for chicken eggshell OPN. Lane 1, total soluble protein extract from decalcified eggshell (1 M HCl); lane 2, acidic eggshell matrix proteins, not retained on CM Sephadex (see Methods). (**B**) Immunohistochemistry (pink) for OPN protein showing its incorporation and distribution throughout the full thickness of the eggshell (decalcified here). Brackets indicate areas in outermost PL with concentrated OPN amounts. (**C**) Immunogold labeling for OPN (arrows) and TEM showing the association of OPN with a lacy network of organic matrix dispersed throughout the PL of the eggshell. (B) and (C) are from demineralized shell samples, resulting in the artifactual partial collapse of an organic matrix structure.

We postulated that regional and local variations in OPN content (and likely other regulatory molecules in the shell) may lead to the differences we observed in nanostructure size that changed from one layer to another. From this, we also surmised that the sites we observed having the 5- to 7-nm nanodomains may contain the highest level of mineralization-inhibiting matrix molecules such as OPN. At these sites, the proteins may exert nanodomain control by binding/sequestering mineral ions and possibly acting to stabilize an ACC precursor phase and by binding to crystallographic faces of calcite. It is also likely that acidic organic matrix molecules fill the internanosubunit volumes that are not crystallized, all of which may contribute to imaging contrast differences observed by TEM that provide visual evidence for nanostructure.

Controlling the nanostructure of synthetic calcite using OPN

To investigate the possibility that OPN might be able to induce nanostructure in synthetic calcium carbonate, calcite crystals were grown in the presence of OPN. After microtoming to expose the interior of the grown synthetic calcite crystals, control calcite (grown without added protein) showed no internal nanostructure, as observed by AFM (Fig. 5A). The same analysis performed on similarly microtome-cut calcite showed an internal nanostructure when calcite was grown in either low (0.9 μM) or high (5.9 μM) OPN concentration (Fig. 5, B and C, respectively). The average (±SD) size (Feret diameter) of the nanostructure induced in the presence of low and high OPN concentration was 77 ± 27 nm and 29 ± 7 nm, respectively (fig. S6A). Nanostructure distribution from the synthetic crystals grown with 0.9 or 5.9 μM OPN is shown in fig. S6 (B and C, respectively). Consistent changes in area measurements for OPN concentration were also observed (fig. S6D). These nanostructural observations, together with the measured change in nanostructure size after growth in different OPN concentrations, demonstrate not only nanostructure induction but also control of nanostructure size by OPN (increasing concentration produces

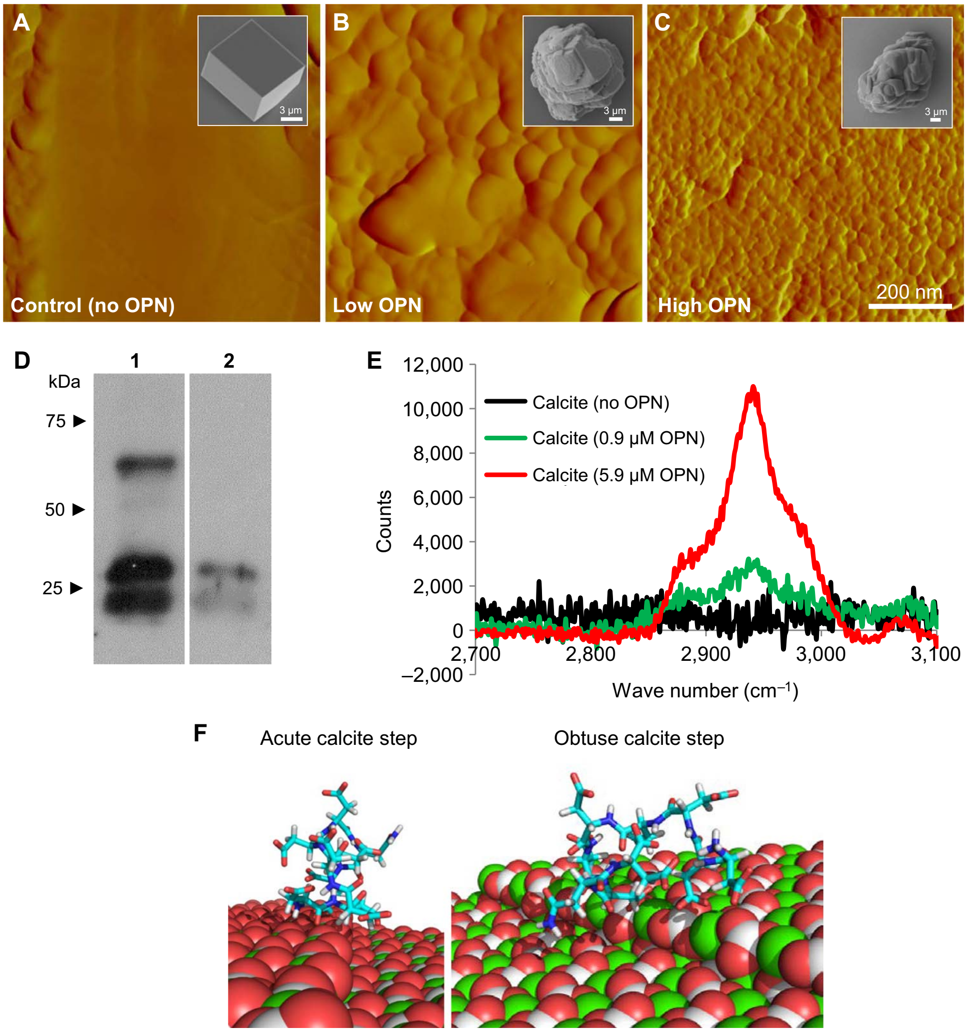

Fig. 5. Nanostructure induced by OPN and protein occlusion within calcite. (**A** to **C**) AFM images of the interior of microtome-cut calcite crystals showing no nanostructure in the absence of OPN (A) but visible nanostructure after growth in the presence of 0.9 μM OPN (B) or 5.9 μM OPN (C) (scanning area, 800 nm × 800 nm). Insets in (A) to (C) show typical SEM images of calcite crystals from which AFM images were obtained after microtoming to expose the interior structure. (**D**) Immunoblotting after gel electrophoresis of dissolved crystals showing retrieved OPN and degraded OPN fragments (lane 1, OPN protein alone; lane 2, dissolved crystals growing in the presence of 5.9 μM). (**E**) Micro-Raman spectra from grown crystals, demonstrating a C–H protein peak. (**F**) Computationally simulated (RosettaSurface) conformer docking of the polyaspartate domain (^{99}DDDDDDDND^{107}) of chicken OPN on the obtuse and acute step of calcite (binding energy, approximately −14 kcal/mol for both cases). Calcite atoms: Ca, green; C, gray/white; O, red.

smaller nanostructure size). HRTEM lattice imaging of a FIB-cut section of a synthetic calcite crystal grown with 5.9 μM OPN (fig. S7A) confirmed the existence of a nanostructure, with the nanocrystals having a significant preferential crystallographic orientation, as shown by SAED (fig. S7B). Notably, the measured nanostructure size from the synthetic calcite grown at the low OPN concentration was similar to the size found in the inner region of the eggshell PL, whereas the higher OPN concentration produced a nanostructure size similar to the outer part of the eggshell in the VCL. TEM of control calcite crystals (grown without added OPN) showed no internal nanostructure (fig. S8). Consistent with this, and as previously shown by others, soluble acidic organic matrix extracted from nacre induces in vitro the formation of nanostructured synthetic calcite crystals (*33*), and Xu *et al.* (*34*) observed a nanocrystalline internal structure and mesoscopic behavior after growing calcite in the presence of copolymers.

As was performed on eggshell, we examined the structure of the synthetic crystals in greater detail after FIB sectioning and HRTEM and electron tomography. Bright-field TEM imaging and tilt-series electron tomography (fig. S9) showed a homogeneous nanostructure in the crystals having a network of small, high-density mineral nanodomains (movies S3 and S4).

As shown in previous studies (*2*, *35*), the significant alterations seen by SEM in external calcite rhombohedral morphology was OPN concentration–dependent (insets in Fig. 5, A to C). Eggshell matrix constituents and uterine fluid extracts and proteins have been previously used to modify calcite growth in vitro. SEM observations of calcite crystals precipitated in the presence of chicken uterine fluid (containing OPN and many other proteins) collected from laying hens at different stages of eggshell formation showed quasi-spherical or rodlike aggregations of calcite microcrystals elongated along the *c* axis (*36*). Although some effects of OPN have been noted in modifying external calcite rhombohedral morphology (*2*), to date, no one has observed that an eggshell matrix protein induces internal nanostructure in calcite.

To verify that our nanostructure observations from the interior regions of the synthetic calcite crystals grown in the presence of OPN were indeed attributable to incorporated protein, we recovered the added OPN from the interior of the crystals. This was carried out by first removing surface-bound protein using NaOH and then dissolving the calcite to make a protein extract. We submitted this extract to gel electrophoresis, from which we identified recovered OPN by immunoblotting and compared it to the state of the originally added protein (Fig. 5D). From the dissolved calcite, we obtained characteristic OPN peptide bands arising from originally occluded, and then retrieved, OPN. Compared to the state of the OPN at the time of addition to the growth system, the retrieved protein extract showed no remaining full-length OPN but only the two smaller OPN peptide bands. This perhaps reflects autocatalytic cleavage of OPN during the occlusion process or site-specific hydrolysis under the basic conditions that can arise in slow-diffusion systems (such as the one we used) or selective occlusion of OPN fragments.

Further confirmation that OPN was occluded into the calcite to generate a nanostructure was obtained from micro-Raman spectroscopy, which showed a broad spectral peak between 2850 and 3000 cm^{-1} for the two OPN concentrations (Fig. 5E). This peak corresponds to C–H vibrational stretching (*37*) observed for proteins, with the peak intensity reflecting the amount of added OPN. Together, these data indicate that OPN occlusion within calcite is part of a process that contributes to the development of calcium-carbonate nanostructures, similar to what we observed in the eggshell.

The influence of OPN on inducing nanostructure and modulating the dimensions of this nanostructure, and its incorporation into calcite, can be largely attributed to its strong binding to mineral occurring through the acidic peptide stretches in its primary amino acid sequence (*38*). We thus computationally modeled, using RosettaSurface (*39*), docking of the highly acidic polyaspartate sequence found in chicken OPN (^{99}DDDDDDDND^{107}) to acute and obtuse growth steps of calcite (Fig. 5F). The binding energies to these two calcite surfaces were equal, being approximately −14 kcal/mol. The fact that these two values are the same indicates that there is no preferred selection between the two steps. This conclusion is supported by the observation of the generally rounded morphology of the nanostructure, as shown by AFM imaging (Fig. 5, B and C).

Functional properties of the nanostructured eggshell

The hardness and elastic modulus behavior of the nanostructured layers of chicken eggshell was investigated by observing their nanoindentation characteristics. Nanoindentation strikes, across the full cross-sectional thickness of fractured eggshell, revealed a gradually decreasing hardness and elastic modulus from the outermost region of the eggshell (the VCL) toward the central region of the PL (Fig. 6, A and B). Further nanoindenting toward the interior side of the shell showed increasing hardness and elastic modulus values toward the innermost ML (Fig. 6, A and B). In correlating the hardness measurements with nanostructure size, the highest hardness values were obtained from the outermost VCL and upper PL where the smallest nanostructure was demonstrated (Fig. 6C). The hardness in nanocrystalline materials, including hard ceramics, is known to inversely increase with a decrease in subunit size (up to a certain critical value), which is a well-known feature of the Hall-Petch relationship. Here, the hardness of materials (H) is dependent on crystal size (d) and is shown by the empirical Hall-Petch equation $H = H_0 + k_{\mathrm{H}}d^{-1/2}$, where H_0 is the hardness of a single crystal and k_{H} is a material-specific constant (*40*). For approximately the outermost half of the shell, our results follow the Hall-Petch model, indicating that eggshell nanostructure, in conjunction with its composition and microarchitecture (*41*), are factors that determines its hardness. In addition, high elastic modulus values were obtained in the outer eggshell layers having the smallest observed nanostructure (VCL and upper PL) and the highest amount of protein including OPN. Similar to other mineralized tissues, it is expected that the tension-shear model (Jaeger-Fratzl model) applies in biocomposites, where the mineral carries the tensile load, whereas the protein transfers the load between the nanomineral units via shear (*14*). Moving from the middle PL into the ML, the inverse correlation of decreasing hardness and elastic modulus did not continue to hold with increasing nanostructure size; for this, we have no explanation other than there potentially being different compositions or less structural homogeneity in these regions, as has been described previously (*2*).

Measurements at the nanoscale of the mechanical properties and their relationship with the size of nanogranular structure complement previous observations on the influence of the structural organization of eggshell at the microscale on its mechanical properties (*41*, *42*). In these studies, an increase in the size of calcitic columnar crystal units in eggshell laid by older hens correlated with a significant reduction in eggshell breaking strength. The abrupt decrease of eggshell mechanical properties after 1 year of laying is a substantial problem for the egg industry, which is actively looking for strategies to extend the laying period of hens while maintaining eggshell quality. Overall, previous and new data show that the mechanical properties of eggshell are controlled

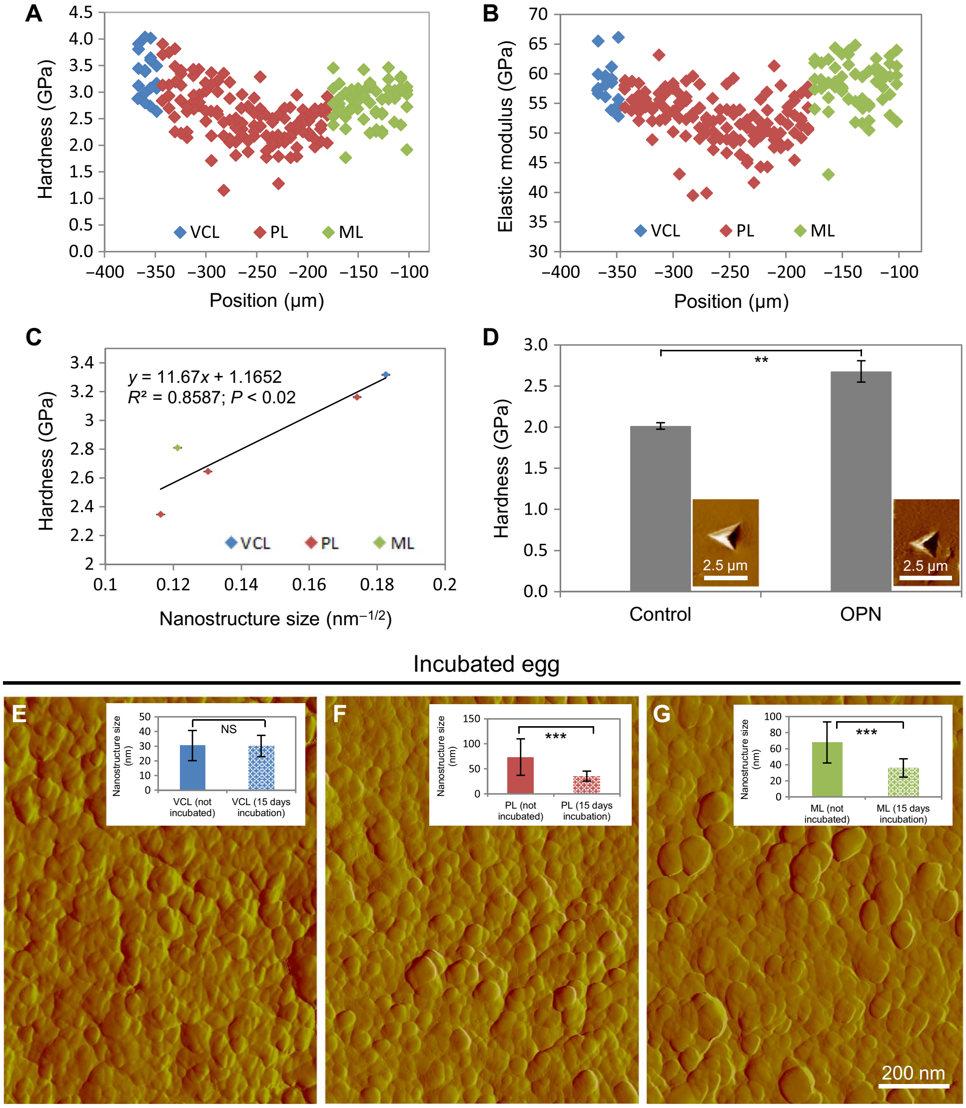

Fig. 6. Mechanical testing by nanoindentation of eggshell and synthetic calcite crystals and effects of physiologic eggshell dissolution. (**A**) Hardness distribution across the eggshell layers. (**B**) Elastic modulus distribution across the eggshell layers. (**C**) Hall-Petch plot of average hardness versus nanostructure size distribution in the eggshell layers. (**D**) Hardness values from synthetic calcite crystals grown in the absence (control) and presence of OPN (5.9 μM). Insets show typical images of residual indents on the specimen surface. Significant difference is indicated by a bracket (**$P < 0.01$). (**E** to **G**) AFM images of nanostructured VCL (E), middle PL (F), and ML (G) eggshell layers from a fertilized egg incubated for 15 days (scanning area, 1.2 μm × 1.2 μm). Insets show nanostructure size distribution of the different eggshell layers, comparing eggs that were not incubated to incubated eggs. No significant difference ($P > 0.05$) is observed between VCLs, whereas a significant difference (***$P < 0.001$) in size exists between the two groups for the PL and the ML. Values were compared by a two-paired Student's *t* test.

by its structural organization over different length scales. Given this context, we assessed by nanoindentation the mechanical properties of the synthetic calcite crystals grown with OPN (5.9 μM). The hardness of these calcite crystals increased significantly with the occlusion of OPN, which induced nanostructure (Fig. 5, A to C, and figs. S8 and S9). The average (±SD) hardness value of the calcite grown without OPN was 2.02 ± 0.04 GPa, whereas the average (±SD) hardness of the calcite crystals grown with added OPN was 2.79 ± 0.1 GPa (Fig. 6D).

Bones, teeth, and shells of all types have remarkable mechanical properties, as conferred by their composite hybrid structure of mineral particles/platelets dispersed within an extended organic framework commonly called the extracellular matrix. In many cases, these biocomposites exhibit levels of hierarchical structure ranging from the nanoscale to the macroscale (*14*), architectures that typically provide toughness to biomineralized structures (*43*, *44*). In essentially all cases, nanometer-length–scale organized structures are important in providing these mechanical properties (*14*), a feature that currently drives bioinspired materials development (*45*). The Griffith criterion describing crack propagation in materials in terms of length scale defines a critical limit below which energy considerations will not allow a crack to propagate further (*46*). For biocomposites (where nanostructure is commonplace), this is considered to ensure optimum fracture strength and maximum tolerance of flaws (*14*). In this case, the Griffith criterion applied to intercalated organics between mineral domains at the nanoscale would describe a distribution of stresses across larger volumes; this would provide a toughening mechanism for function that acts to decrease crack propagation in organismal biomineralized structures. In nacre, as another example, Wang *et al.* (*47*) reported that cracks deflect and propagate within the nanostructured tablets along the location of occluded organics, following an undulating intergranular crack path. Together, these and other studies show that nanostructure and the incorporation of organics (*48*) lead to enhanced mechanical properties for biomineralized structures.

Apart from contributing to mechanical properties, we hypothesized that the increased surface area afforded by the small mineral nanodomains in the inner layers of the eggshell makes more surface area available for the mineral dissolution—a process that provides calcium to the developing chick embryo primarily for skeletal growth. In principle, such a process would allow retention of overall shell layer structure but with some thinning and compromised strength, a feature ultimately necessary for successful chick pipping to puncture/break the shell during hatching. To explore this possibility, we examined the shell nanostructure of fertilized eggs incubated for 15 days (chick hatching typically occurs around 21 days of incubation). AFM of these shells revealed that, although the VCL nanostructure remained unaffected [30 ± 7 (SD) nm] as we surmised (Fig. 6E), there was a significant decrease in nanostructure size (Feret diameters) from this physiologic mineral dissolution in the innermost region of the PL [36 ± 10 (SD) nm] (Fig. 6F) and in the ML [36 ± 11 (SD) nm] (Fig. 6G), and changes in nanostructure area measurements of the same regions were consistent with the changes in diameter values (fig. S2, B to D). At the microscale and macroscale, inner shell dissolution during egg incubation occurs in the mammillae and at the base plate below the tips of the mammillary knobs, the latter dissolution resulting in detachment of the shell from the outer eggshell membranes (*49*). Moreover, at the ultrastructural and microstructural level, the inner part of the eggshell (ML) consists of much smaller (narrower) calcite crystals compared to the bulk eggshell material that consists of larger (wider) columnar calcite units (*50*); the organization at this level could be a determinant for dissolution of the eggshell.

Related to this physiologic eggshell dissolution, in terms of the stability of nanocrystals in aqueous environments, where nanostructure size is very small as in the VCL, crystallite size can be preserved when that size correlates with a certain critical value of undersaturation conditions for a particular mineral (*51*). Under these critical conditions, the dissolution rate of the nanocrystallites can be self-inhibited, in contrast to the Ostwald-Freundlich scenario, which usually assumes that smaller particles are dissolved faster because of their higher solubility. Thus, the smallest nanostructure observed by AFM, appearing in the outermost region of the VCL, can partly explain eggshell resistance to dissolution under external aqueous (including environmental) conditions. In addition, occluded pericrystal organic material accumulating at nanograin boundaries can reduce their solubility and control the dissolution of biocomposites (*52*). Consequently, nanostructured biominerals can even remain stable in undersaturated biological and other aqueous fluids and remain comparatively resistant to dissolution phenomena (*51*), which is clearly an evolutionary advantage for humid/wet, egg-incubation conditions.

Together, the information we report here on the functional properties of nanostructured eggshell provides insight into biomineralization mechanisms and eggshell mechanical properties. Moreover, the findings also potentially serve to inform rational designs for novel, bioinspired functional nanomaterials having desirable and tunable unique properties.

CONCLUSIONS

Here, the nanostructure of mineralized avian (chicken) eggshell *G. gallus* is described across the entire thickness of the shell for each of its major layers. Nanostructure size is different for each of the layers, presumably arising from the effects on mineralization of incorporated organic molecules. Using one such shell-resident biomolecule, the protein OPN, a synthetic calcite nanostructure can be induced, and its size can be controlled by the addition of this inhibitory, mineral-binding shell protein; higher concentrations of OPN lead to a smaller nanostructure size. In the outer half of the eggshell, decreased nanostructure size generally correlates with increased shell hardness, an observation reproduced by growing synthetic calcite crystals in the presence of OPN. In fertilized incubated eggs, partial dissolution of calcitic nanostructure occurs in the inner region of the shell, providing calcium for the growing chick embryo skeleton and resulting in the shell weakening required for hatching. These findings provide insight into chicken eggshell formation, mechanical function, and dissolution, and they can be used to inform design concepts for synthetic nanocomposites having novel properties.

MATERIALS AND METHODS

Materials

Eggshells

The total number of White Leghorn domestic chicken (*G. gallus*) eggs studied for these results was 30 (this includes unfertilized and fertilized incubated eggs). For each data set collected, at least two to six shell fragments from different eggs were examined by the respective methodologies; all results were reproducible, and we will show typical examples. Eggshells were prepared according to the method described by Chien *et al.* (*2*, *49*). Briefly, eggshells were washed with physiologic saline (150 mM sodium chloride solution) and double-distilled water and air-dried at room temperature. A portion of the air-dried or fixed (and sometimes demineralized) shell fragments, removed from the equatorial region of the eggshell, were embedded in LR white acrylic resin (London Resin Company) for microtome sectioning and microscopy analyses. In addition, shell cross sections of approximately 100 μm in thickness were cut using a diamond saw rotating disc (model VC-50 Precision Diamond Saw, LECO).

Chemicals and OPN

For crystallization experiments, anhydrous calcium chloride ($CaCl_2$) was purchased from Thermo Fisher Scientific, and ammonium carbonate [$(NH_4)_2CO_3$] was purchased from Sigma-Aldrich. Bovine phosphorylated milk OPN (with approximately 24 phosphorylations per molecule) was provided by Arla Foods and was prepared according to the method described by Sørensen and Petersen (*53*).

Methods

Atomic force microscopy

AFM was conducted on eggshell fragments that were cut with a diamond saw and polished across a series of water stones from rough 1000 grit to fine 13,000 grit (Lee Valley Company), followed by ultrasonication and washing. Height and amplitude images were taken using a Nanoscope IIIa (Veeco) operating in tapping mode at room temperature in air, using a vertical-engage E scanner and NanoScope version 5.30 software (Veeco/Bruker-AXS Inc.). V-shaped tapping mode probes (typical tip apex radius of approximately 7 nm) with Si cantilevers having a spring constant $k = 42$ N/m (Bruker-AXS Inc.) were used. To reduce imaging artifacts, the tip force exerted on the surface was optimized by the amplitude set point being as high as possible. The Feret diameters and area measurements of the units comprising the nanostructure observed by AFM were calculated using ImageJ software. At least 100 Feret diameters and 100 area measurements of the nanostructure of each eggshell layer from fertilized incubated and nonincubated eggs, as well as from each synthetic calcite crystal grown in the presence of OPN (0.9 and 5.9 μM), were calculated from AFM images (obtained using amplitude mode) after performing high-pass processing to enhance boundaries.

Scanning electron microscopy

Examination of the external morphology of synthetic calcite crystals grown with or without OPN was performed using an FEI Inspect F-50 FE-SEM (FEI Company) operating in high-vacuum mode at 5 kV. For eggshell nanostructure observations, samples were sputter-coated with an approximately 2-nm Cr layer using an EMS150T Turbo-Pumped Sputter Coater.

FIB sectioning for TEM

Approximately 80-nm-thick sections (lamellae) were prepared using a dual-beam FIB microscope (FEI Helios 600 NanoLab, FEI) equipped with a gallium ion source. Samples were mounted on aluminum SEM stubs and coated with a 2-nm platinum layer. For the ion-beam preparation, a rectangular section (2 μm thick) of a Pt protection layer was deposited on the area of interest, after which an eggshell slab with a thickness of 2 μm was milled by the ion beam, and the section was transferred for the final thinning onto a copper TEM half-grid using an EasyLift nanomanipulator. The lift-out section was further milled at 30 kV and 9.4 nA, and final thinning was carried out at 30 kV and 0.77 nA to reach a thickness of 80 to 100 nm.

Wedge polishing for TEM

Electron-transparent wedge-shaped thin sections of eggshells were prepared on a MultiPrep precision polishing system (Allied High Tech) using a waning series of micrometer-sized diamond polishing films (from 30 mm down to 0.1 mm; Allied High Tech) while obeying the rule of the "trinity of damage" [see the study of Hovden *et al.* (*18*)]. A nonaqueous lubricant (DP-Lubricant Brown) was used to prevent mineral dissolution. Samples were fixed onto a Pyrex-polishing stub (Allied High Tech) with Loctite Super Glue (Henkel AG & Co. KGaA), allowing gentle removal later by means of an acetone bath. The convex side of the eggshell was polished at an angle of 10° until all the different mineral layers were visible at the sample's edges. The sample was then carefully removed from the stub, flipped upside down, and again polished under an angle of 2° using a waning series of lapping films. As soon as the tip of the wedge-shaped sample showed fringes, the sample was carefully removed from the stub and mounted to an annular molybdenum TEM grid (Plano GmbH) with M-Bond 610 epoxy (VPG).

Transmission electron microscopy

HRTEM was performed to examine crystal lattice fringes on thin (~80 nm) FIB sections of eggshell and of synthetic calcite crystals grown in vitro with (or without) OPN. TEM images using the bright-field mode, as well as SAED patterns, were acquired using a FEI Tecnai G^2 F20 microscope operating at 200 kV equipped with a Gatan UltraScan 4000 charge-coupled device (CCD) camera model 895 and an aperture of either 1 or 270 nm. Images were recorded under a Scherzer defocus condition of ~67 nm.

Optical microscopy

To analyze the eggshell microstructure using a polarized light microscope (Nikon LZM 1000), thin eggshell cross sections were prepared by embedding eggshells in epoxy resin (Buehler Epothin), cutting them with a low-speed diamond saw, mounting them on a glass slide, and polishing them down to less than 30 μm.

Electron backscatter diffraction

High-resolution EBSD maps of the chicken eggshell microstructure were obtained from thin, polished eggshell cross sections coated with carbon. The EBSD maps were collected over 20 hours using an Auriga Zeiss scanning electron microscope and a 0.3-μm-step size resolution. All EBSD data were collected and analyzed with the AZtec 2.1 software (Oxford Instruments).

2D XRD

The microstructure of the eggshell was analyzed on polished eggshell cross sections (0.4 mm thick) with a Bruker D8 VENTURE x-ray single crystal diffractometer equipped with a photon area detector using a molybdenum microsource. The eggshell cross sections were analyzed in transmission mode, with the sample oriented perpendicular to the x-ray beam. A series of frames were registered while rotating the sample in φ angle within the 3° to 10° angular range using 0.3° steps.

Electron tomography

FIB-cut sections approximately 80 nm thick from eggshell and synthetic calcite crystals grown with 5.9 μM OPN were collected on a copper grid. A series of single–axis tilt images was collected with a Tecnai G^2 F20 cryo-S/TEM (FEI) operated at an accelerating voltage of 200 kV equipped with a Gatan UltraScan 4000 4k × 4k digital CCD camera system (model 895). Images were captured at a magnification of 62,000 over a tilt range of −40° to +60° for the eggshell samples and −50° to +50° for the synthetic calcite crystals (2° increments in both low tilts and high tilts on the 80-nm-thick sections). The resulting images had pixel sizes of 0.19 nm. The images from the tilt series were aligned, filtered, and reconstructed into a tomogram using the IMOD software package (*54*). The movies for the raw tilt series and reconstruction were carried out using IMOD, whereas the movies with 3D volume with solid and surface rendering were generated using UCSF Chimera (version 1.10.1).

Nanoindentation hardness testing

Nanoindentation testing was carried out using a Hysitron Ubi III system with 1D transducer mounted to a piezoelectric scanner capable of surface imaging similar to AFM. A Berkovich diamond tip of 50-nm defect radius was used for indentation and surface imaging. Nanoindentation was performed across the eggshell thickness using a matrix consisting of five rows of 83 indents spaced at 50 μm in the lateral direction and 6 μm in the vertical direction. The peak load was 5 mN, and the loading/unloading function consisted of 5-s loading, 2-s hold time, and 5-s unloading. All indentation tests were carried out in triplicate on three eggshell sections. For nanoindentation tests on the synthetic crystals, cold polymerizing epoxy resin was poured over glass coverslips having attached calcite crystals grown in the absence (control) and presence of OPN (5.9 μM). The glass coverslips were removed after resin hardening, leaving behind a flat surface with exposed, resin-embedded calcite crystals. The crystal surface was prescanned, and images (10 μm × 10 μm area) were acquired, which allowed for the identification of the desired location for indentation. The indentation test was carried out using several partial-unloading steps starting at 0.3 mN peak load, followed by 0.6, 1, 2, and 3 mN to a maximum peak load of 5 mN. A total number of six loading/unloading cycles were used to nanoindent 10 synthetic calcite crystals for each condition. After each indentation test, an image was acquired to determine where the indent was placed and indentation features. A correction for the compliance of the resin was applied using Matlab software, which was based on techniques similar to those carried out by Buchheit and Vogler (*55*) and Leggoe (*56*). Analysis of the load-depth curves obtained from indentation was carried out using the Oliver and Pharr method (*57*). Figure S10 shows typical nanoindentation displacement curves for eggshell and synthetic calcite crystals grown in OPN (5.9 μM).

Immunodetection of OPN in eggshell

Eggshell powder (100 g) was demineralized in 1 M HCl and partially purified by sequential chromatography on CM Sephadex and DEAE-Sephadex resins (*5*). Samples containing total extracted OPN [lane 1, soluble acid extract; lane 2, void volume not retained by CM Sephadex in 0.3 M NaCl and 25 mM Na acetate (pH 4.0)] were separated by SDS–polyacrylamide gel electrophoresis (PAGE) on a 10% gel and transferred to nitrocellulose membrane for immunoblotting, as previously described (*5*), with a rabbit antiserum raised to chicken OPN residues 1 to 11.

For light microscopy immunohistochemistry, eggshells demineralized in EDTA containing 0.1% glutaraldehyde were embedded in paraffin, and 5-μm-thick sections were immunostained for OPN using a rabbit anti-chicken OPN polyclonal antibody (antibody courtesy of L. C. Gerstenfeld, Boston University). Deparaffinized sections were treated with 1% bovine testicular hyaluronidase (Sigma-Aldrich) for 30 min at 37°C, followed by incubation with anti-OPN antibody diluted 1:200 in 5% normal goat serum/0.2% bovine serum albumin (BSA) in tris-buffered saline (TBS) with 0.01% Tween 20 (TBS-T) [50 mM tris-HCl, 150 mM NaCl, and 0.01% Tween 20 (pH 7.6)]. Sections were washed and incubated with secondary biotinylated goat anti-rabbit immunoglobulin G (Caltag Laboratories, Invitrogen), and then the VECTASTAIN ABC-AP kit (Vector Laboratories) was applied. Optical micrographs were obtained using a Leitz DMRBE (Leica) and a DXC-950 3-CCD camera (Sony). ImageJ software and line scans across the eggshell thickness after immunostaining were used to compare OPN staining intensity in the different shell layers. More specifically, seven staining intensity-profile, linear plot views from OPN-immunostained eggshell sections that include all eggshell layers (VCL, PL and ML) were used. Each linear plot shows the local staining intensity along a line drawn perpendicular to the eggshell surface. Profile plots were normalized to the background noise level and averaged.

For immunogold labeling of OPN at the ultrastructural level, eggshell fragments demineralized in EDTA containing 0.1% glutaraldehyde were embedded in LR white resin and sectioned at 80 nm using an ultramicrotome, and grid-mounted sections were incubated with anti-chicken OPN antibody, as described previously (*2*). Immunolabeling reactions were visualized by incubation with the protein A–colloidal gold complex (14-nm gold particles; G. Posthuma, University of Utrecht), followed by conventional staining with uranyl acetate and lead citrate. TEM of these sections was performed as described above.

Synthetic calcite growth in the presence of OPN

Calcite crystals were synthesized by ammonium carbonate diffusion into a 10 mM $CaCl_2$ solution with (or without) added OPN (0.9 and 5.9 μM). Calcite crystallization took place over 2 hours on glass coverslips in small wells contained within a well sealed desiccator previously charged with 1 g of $(NH_4)_2CO_3$ powder. At the end of each experiment, the glass coverslips were removed from solution, gently rinsed with distilled water and ethanol, and air-dried for further characterization. All experiments were performed at least in triplicate.

To assess OPN occlusion within the calcite crystals, the OPN-grown calcite crystals were dissolved in 5% acetic acid for 10 min after removing any surface-bound protein using 1 M NaOH. SDS-PAGE was performed on a 10% gel, and protein/peptide bands were transferred to a polyvinylidene difluoride (PVDF) membrane and blocked using a 5% BSA solution in TBS-T. The PVDF membrane was probed with a rabbit anti-bovine OPN in 5% BSA/TBS-T, followed by visualization using enhanced chemiluminescence reagent.

For microtoming to reveal the interior structure by AFM of the crystals grown with or without OPN, glass coverslips with adherent crystals were embedded in epoxy resin (Epon, Electron Microscopy Sciences) blocks, the glass coverslips were fractured off, and the crystals were sectioned using an ultramicrotome (Leica).

Raman spectroscopy

To investigate the incorporation of OPN inside the calcite crystals, we performed micro-Raman spectroscopy using a Renishaw inVia Raman microscope (Renishaw) equipped with a holographic spectrometer and a Leica DM2500 M optical microscope (Leica Microsystems GmbH). The excitation source was a 514.5-nm argon laser with a laser spot size of approximately 2 μm and an excitation power of 25 mW. The laser was focused through a 50× objective having a numerical aperture of 0.75 on single crystals, as grown on a glass coverslip. Each Raman spectrum was typically acquired for 10 s, and 10 scans were accumulated for each measurement to minimize noise effects. Several spot analyses were taken from each selected area to confirm the spectral reproducibility. For the detection of incorporated OPN into the calcite, all crystals were washed with 1 M NaOH for 2 min to remove surface-bound OPN. The spectra were acquired at room temperature with a spectral resolution of 1 cm^{-1}. Calibration was performed using the 520.5-cm^{-1} band of a silicon wafer as a standard. Renishaw WiRE 3.4 (Windows-based Raman Environment) software was used for Raman data acquisition.

Computational simulation

To predict the binding energies and geometries of the polyaspartate domain of chicken OPN on the obtuse and acute steps of the calcite (104) surface, we used the RosettaSurface algorithm (*39*). The standard algorithm was modified to account for the asymmetry introduced by step edges and to model a flexible peptide, as outlined by Pacella *et al.* (*39*). We constructed an extended nine–amino acid chicken OPN peptide having the sequence ^{99}DDDDDDDND^{107} using ideal bond lengths and angles (*58*). We constructed a calcite (104) slab using unit cell coordinates from Graf (*59*), and obtuse and acute step edges were created by removing a layer of atoms along the appropriate edge directions. We calculated adsorption energies on both the acute and obtuse step edges using the Talari-2013 energy function (*60*), which includes a linear combination of terms for van der Waals energies, hydrogen bonds, electrostatics, and solvation via an implicit-solvent Gaussian exclusion model. We used energy function parameters from Raiteri *et al.* (*61*) for the atoms of the calcite step edges. For both the acute and obtuse step edges, we generated 20,000 candidate structures and selected the lowest-scoring structures for energetic analysis.

Statistical analysis

Statistical analysis of the samples was performed using a two-tailed Student's *t* test. Measurements were considered statistically significant when the *P* value was less than 0.05.

SUPPLEMENTARY MATERIALS

Supplementary material for this article is available at http://advances.sciencemag.org/cgi/content/full/4/3/eaar3219/DC1

fig. S1. Distribution of measured eggshell nanostructures by AFM.

fig. S2. Eggshell nanostructure area measurements.

fig. S3. Internal nanocrystal misalignments in the PL of chicken eggshell.

fig. S4. TEM showing eggshell nanostructure.

fig. S5. Semiquantification of OPN immunostaining across the eggshell thickness.

fig. S6. Effect of OPN on nanostructure size in synthetic calcite crystals.
fig. S7. OPN induces nanostructure in synthetic calcite crystals.
fig. S8. Absence of nanostructure in synthetic control calcite crystal (no added OPN).
fig. S9. Electron microscopy of a FIB section showing nanostructure in a synthetic calcite crystal grown with OPN (5.9 μM).
fig. S10. Nanoindentation displacement curves for eggshell and synthetic calcite crystals grown in OPN (5.9 μM).
movie S1. 3D reconstruction from a tilt series of the upper PL of avian chicken eggshell *G. gallus*.
movie S2. 3D reconstruction of nanodomains found in the upper PL of the eggshell.
movie S3. 3D reconstruction from a tilt series of the synthetic calcite crystal grown with 5.9 μM OPN.
movie S4. 3D reconstruction of a nanostructured region found in the synthetic calcite crystal grown with 5.9 μM OPN.

REFERENCES AND NOTES

1. Y. Nys, M. T. Hincke, J. L. Arias, J. M. Garcia-Ruiz, S. E. Solomon, Avian eggshell mineralization. *Poult. Avian Biol. Rev.* **10**, 143–166 (1999).
2. Y.-C. Chien, M. T. Hincke, H. Vali, M. D. McKee, Ultrastructural matrix–mineral relationships in avian eggshell, and effects of osteopontin on calcite growth *in vitro*. *J. Struct. Biol.* **163**, 84–99 (2008).
3. K. Mann, B. Maček, J. V. Olsen, Proteomic analysis of the acid-soluble organic matrix of the chicken calcified eggshell layer. *Proteomics* **6**, 3801–3810 (2006).
4. K. Mann, J. V. Olsen, B. Maček, F. Gnad, M. Mann, Phosphoproteins of the chicken eggshell calcified layer. *Proteomics* **7**, 106–115 (2007).
5. M. T. Hincke, C. P. Tsang, M. Courtney, V. Hill, R. Narbaitz, Purification and immunochemistry of a soluble matrix protein of the chicken eggshell (ovocleidin 17). *Calcif. Tissue Int.* **56**, 578–583 (1995).
6. M. Pines, V. Knopov, A. Bar, Involvement of osteopontin in egg shell formation in the laying chicken. *Matrix Biol.* **14**, 765–771 (1995).
7. L. W. Fisher, D. A. Torchia, B. Fohr, M. F. Young, N. S. Fedarko, Flexible structures of SIBLING proteins, bone sialoprotein, and osteopontin. *Biochem. Biophys. Res. Commun.* **280**, 460–465 (2001).
8. L. Kalmar, D. Homola, G. Varga, P. Tompa, Structural disorder in proteins brings order to crystal growth in biomineralization. *Bone* **51**, 528–534 (2012).
9. G. K. Hunter, J. O'Young, B. Grohe, M. Karttunen, H. A. Goldberg, The flexible polyelectrolyte hypothesis of protein-biomineral interaction. *Langmuir* **26**, 18639–18646 (2010).
10. H. A. Lowenstam, S. Weiner, *On Biomineralization* (Oxford Univ. Press, 1989).
11. J. J. De Yoreo, P. U. P. A. Gilbert, N. A. J. M. Sommerdijk, R. L. Penn, S. Whitelam, D. Joester, H. Zhang, J. D. Rimer, A. Navrotsky, J. F. Banfield, A. F. Wallace, F. M. Michel, F. C. Meldrum, H. Cölfen, P. M. Dove, Crystallization by particle attachment in synthetic, biogenic, and geologic environments. *Science* **349**, aaa6760 (2015).
12. S. E. Wolf, C. F. Böhm, J. Harris, B. Demmert, D. E. Jacob, M. Mondeshki, E. Ruiz-Agudo, C. Rodríguez-Navarro, Nonclassical crystallization in vivo et in vitro (I): Process-structure-property relationships of nanogranular biominerals. *J. Struct. Biol.* **196**, 244–259 (2016).
13. G. Falini, S. Albeck, S. Weiner, L. Addadi, Control of aragonite or calcite polymorphism by mollusk shell macromolecules. *Science* **271**, 67–69 (1996).
14. H. Gao, B. Ji, I. L. Jäger, E. Arzt, P. Fratzl, Materials become insensitive to flaws at nanoscale: Lessons from nature. *Proc. Natl. Acad. Sci. U.S.A.* **100**, 5597–5600 (2003).
15. G. Wu, K.-C. Chan, L. Zhu, L. G. Sun, J. Lu, Dual-phase nanostructuring as a route to high-strength magnesium alloys. *Nature* **545**, 80–83 (2017).
16. A. Pérez-Huerta, Y. Dauphin, Comparison of the structure, crystallography and composition of eggshells of the guinea fowl and graylag goose. *Zoology (Jena)* **119**, 52–63 (2016).
17. J. Seto, Y. Ma, S. A. Davis, F. Meldrum, A. Gourrier, Y.-Y. Kim, U. Schilde, M. Sztucki, M. Burghammer, S. Maltsev, C. Jäger, H. Cölfen, Structure-property relationships of a biological mesocrystal in the adult sea urchin spine. *Proc. Natl. Acad. Sci. U.S.A.* **109**, 3699–3704 (2012).
18. R. Hovden, S. E. Wolf, M. E. Holtz, F. Marin, D. A. Muller, L. A. Estroff, Nanoscale assembly processes revealed in the nacroprismatic transition zone of *Pinna nobilis* mollusc shells. *Nat. Commun.* **6**, 1–7 (2015).
19. A. B. Rodríguez-Navarro, P. Marie, Y. Nys, M. T. Hincke, J. Gautron, Amorphous calcium carbonate controls avian eggshell mineralization: A new paradigm for understanding rapid eggshell calcification. *J. Struct. Biol.* **190**, 291–303 (2015).
20. P. Dalbeck, M. Cusack, Crystallography (electron backscatter diffraction) and chemistry (electron probe microanalysis) of the avian eggshell. *Cryst. Growth Des.* **6**, 2558–2562 (2006).
21. S. Weiner, L. Addadi, Crystallization pathways in biomineralization. *Annu. Rev. Mater. Res.* **41**, 21–40 (2011).
22. A. Gal, S. Weiner, L. Addadi, A perspective on underlying crystal growth mechanisms in biomineralization: Solution mediated growth versus nanosphere particle accretion. *Cryst. Eng. Comm.* **17**, 2606–2615 (2015).
23. L. B. Gower, Biomimetic model systems for investigating the amorphous precursor pathway and its role in biomineralization. *Chem. Rev.* **108**, 4551–4627 (2008).
24. S. E. G. Wolf, L. B. Gower, Challenges and perspectives of the polymer-induced liquid-precursor process: The pathway from liquid-condensed mineral precursors to mesocrystalline products in new perspectives on mineral nucleation and growth, in *New Perspectives on Mineral Nucleation and Growth*, A. E. S. van Driessche, M. Kellermeier, L. G. Benning, D. Gebauer, Eds. (Springer, 2017), pp. 43–75.
25. D. Lammie, M. M. Bain, T. J. Wess, Microfocus X-ray scattering investigations of eggshell nanotexture. *J. Synchrotron Radiat.* **12**, 721–726 (2005).
26. A. M. Turing, The chemical basis of morphogenesis. *Philos. Trans. R. Soc. B* **237**, 37–72 (1952).
27. A. D. Economou, A. Ohazama, T. Porntaveetus, P. T. Sharpe, S. Kondo, M. A. Basson, A. Gritli-Linde, M. T. Cobourne, J. B. Green, Periodic stripe formation by a Turing mechanism operating at growth zones in the mammalian palate. *Nat. Genet.* **44**, 348–351 (2012).
28. A. Verch, I. E. G. Morrison, R. van de Locht, R. Kröger, In situ electron microscopy studies of calcium carbonate precipitation from aqueous solution with and without organic additives. *J. Struct. Biol.* **183**, 270–277 (2013).
29. T. Bánsági, V. K. Vanag, I. R. Epstein, Tomography of reaction-diffusion microemulsions reveals three-dimensional turing patterns. *Science* **331**, 1309–1312 (2011).
30. Y.-C. Chien, M. T. Hincke, M. D. McKee, Avian eggshell structure and osteopontin. *Cells Tissues Organs* **189**, 38–43 (2009).
31. M. T. Hincke, Y.-C. Chien, L. C. Gerstenfeld, M. D. McKee, Colloidal-gold immunocytochemical localization of osteopontin in avian eggshell gland and eggshell. *J. Histochem. Cytochem.* **56**, 467–476 (2008).
32. P. Marie, V. Labas, A. Brionne, G. Harichaux, C. Hennequet-Antier, Y. Nys, J. Gautron, Quantitative proteomics and bioinformatic analysis provide new insight into protein function during avian eggshell biomineralization. *J. Proteomics* **113**, 178–193 (2015).
33. Y.-H. Tseng, C. Chevallard, Y. Dauphin, P. Guenoun, $CaCO_3$ nanostructured crystals induced by nacreous organic extracts. *Cryst. Eng. Comm.* **16**, 561–569 (2014).
34. A.-W. Xu, M. Antonietti, S.-H. Yu, H. Cölfen, Polymer-mediated mineralization and self-similar mesoscale-organized calcium carbonate with unusual superstructures. *Adv. Mater.* **20**, 1333–1338 (2008).
35. M. N. Hong, K. T. Moreland, J. Chen, H. H. Teng, R. Thalmann, J. J. De Yoreo, Effect of otoconial proteins fetuin A, osteopontin, and otoconin 90 on the nucleation and growth of calcite. *Cryst. Growth Des.* **15**, 129–136 (2015).
36. M. T. Hincke, Y. Nys, J. Gautron, K. Mann, A. B. Rodriguez-Navarro, M. D. McKee, The eggshell: Structure, composition and mineralization. *Front. Biosci.* **17**, 1266–1280 (2012).
37. K. M. Bromley, R. Lakshminarayanan, M. Thompson, S. B. Lokappa, V. A. Gallon, K. R. Cho, S. R. Qiu, J. Moradian-Oldak, Amelogenin processing by MMP-20 prevents protein occlusion inside calcite crystals. *Cryst. Growth Des.* **12**, 4897–4905 (2012).
38. J. Sodek, B. Ganss, M. D. McKee, Osteopontin. *Crit. Rev. Oral Biol. Med.* **11**, 279–303 (2000).
39. M. S. Pacella, D. C. E. Koo, R. A. Thottungal, J. J. Gray, Using the RosettaSurface algorithm to predict protein structure at mineral surfaces. *Method Enzymol.* **532**, 343–366 (2013).
40. J. Musil, D. Rostislav, *Novel Nanocomposite Coatings: Advances and Industrial Applications* (Pan Stanford, 2013).
41. A. Rodríguez-Navarro, O. Kalin, Y. Nys, J. M. Garcia-Ruiz, Influence of the microstructure on the shell strength of eggs laid by hens of different ages. *Brit. Poult. Sci.* **43**, 395–403 (2002).
42. A. M. H. Ahmed, A. B. Rodriguez-Navarro, M. L. Vidal, J. Gautron, J. M. García-Ruiz, Changes in eggshell mechanical properties, crystallographic texture and in matrix proteins induced by moult in hens. *Brit. Poult. Sci.* **46**, 268–279 (2005).
43. R. Menig, M. H. Meyers, M. A. Meyers, K. S. Vecchio, Quasi-static and dynamic mechanical response of *Strombus gigas* (conch) shells. *Mat. Sci. Eng. A* **297**, 203–211 (2001).
44. P. Fratzl, R. Weinkamer, Nature's hierarchical materials. *Prog. Mater. Sci.* **52**, 1263–1334 (2007).
45. F. Nudelman, N. A. J. M. Sommerdijk, Biomineralization as an inspiration for materials chemistry. *Angew. Chem. Int. Edit.* **51**, 6582–6596 (2012).
46. A. A. Griffith, The phenomena of rupture and flow in solids. *Philos. Trans. R. Soc. A* **221**, 163–198 (1920).
47. S. Wang, X. Zhu, Q. Li, R. Wang, X. Wang, Damage-tolerance strategies for nacre tablets. *J. Struct. Biol.* **194**, 199–204 (2016).
48. Y.-Y. Kim, J. D. Carloni, B. Demarchi, D. Sparks, D. G. Reid, M. E. Kunitake, C. C. Tang, M. J. Duer, C. L. Freeman, B. Pokroy, K. Penkman, J. H. Harding, L. A. Estroff, S. P. Baker, F. C. Meldrum, Tuning hardness in calcite by incorporation of amino acids. *Nat. Mater.* **15**, 903–910 (2016).

49. Y.-C. Chien, M. T. Hincke, M. D. McKee, Ultrastructure of avian eggshell during resorption following egg fertilization. *J. Struct. Biol.* **168**, 527–538 (2009).
50. A. B. Rodríguez-Navarro, A. Yebra, Y. Nys, C. Jimenez-Lopez, J. M. Garcia-Ruiz, Analysis of avian eggshell microstructure using X-ray area detectors. *Eur. J. Mineral.* **19**, 391–398 (2007).
51. R. K. Tang, L. Wang, C. A. Orme, T. Bonstein, P. J. Bush, G. H. Nancollas, Dissolution at the nanoscale: Self-preservation of biominerals. *Angew. Chem. Int. Ed.* **43**, 2697–2701 (2004).
52. V. Nelea, Y.-C. Chien, J. Paquette, M. D. McKee, Effects of full-length phosphorylated osteopontin and constituent acidic peptides and amino acids on calcite dissolution. *Cryst. Growth Des.* **14**, 979–987 (2014).
53. E. S. Sørensen, T. E. Petersen, Purification and characterization of three proteins isolated from the proteose peptone fraction of bovine-milk. *J. Dairy Res.* **60**, 189–197 (1993).
54. J. R. Kremer, D. N. Mastronarde, J. R. McIntosh, Computer visualization of three-dimensional image data using IMOD. *J. Struct. Biol.* **116**, 71–76 (1996).
55. T. E. Buchheit, T. J. Vogler, Measurement of ceramic powders using instrumented indentation and correlation with their dynamic response. *Mech. Mater.* **42**, 599–614 (2010).
56. J. W. Leggoe, Determination of the elastic modulus of microscale ceramic particles via nanoindentation. *J. Mater. Res.* **19**, 2437–2447 (2004).
57. W. C. Oliver, G. M. Pharr, An improved technique for determining hardness and elastic modulus using load and displacement sensing indentation experiments. *J. Mater. Res.* **7**, 1564–1583 (1992).
58. R. A. Engh, R. Huber, Accurate bond and angle parameters for X-ray protein-structure refinement. *Acta Crystallogr. A* **47**, 392–400 (1991).
59. D. L. Graf, Crystallographic tables for the rhombohedral carbonates. *Am. Mineral.* **46**, 1283–1316 (1961).
60. M. J. O'Meara, A. Leaver-Fay, M. D. Tyka, A. Stein, K. Houlihan, F. DiMaio, P. Bradley, T. Kortemme, D. Baker, J. Snoeyink, B. Kuhlman, Combined covalent-electrostatic model of hydrogen bonding improves structure prediction with Rosetta. *J. Chem. Theory Comput.* **11**, 609–622 (2015).
61. P. Raiteri, J. D. Gale, D. Quigley, P. M. Rodger, Derivation of an accurate force-field for simulating the growth of calcium carbonate from aqueous solution: A new model for the calcite-water interface. *J. Phys. Chem. C* **114**, 5997–6010 (2010).

Acknowledgments: We are grateful to D. Liu, L. Mongeon, L. Malynowsky, Q. Wu, and K. Sears for assistance with TEM and FIB work. We also thank Y. Nakano for her help with the immunohistochemistry experiments, E. Sørensen and Arla Foods for donating OPN protein, L. C. Gernstenfeld for the OPN antibody, A. Ryan for providing eggshell samples, and N. Reznikov for her thoughts on Turing patterns. The assistance of A. Gonzalez and J. Romero (Centro de Instrumentacion Cientifica Universidad de Granada) for the 2D XRD and EBSD analyses is acknowledged. We thank A. Saeed for the use of the Matlab code used for analysis of partial unloading data and compliance corrections. Electron microscopy was performed at McGill University's Facility for Electron Microscopy Research. **Funding:** This work was supported by a grant from the Canadian Institutes of Health Research (no. MOP-142330) and the Natural Sciences and Engineering Research Council of Canada (NSERC; no. RGPIN-2016-05031) to M.D.M., an NSERC (no. RGPIN-2016-04410) Discovery grant to M.T.H., a Spanish Government grant (CGL2015-64683-P) to A.B.R.-N., an Emmy Noether research grant from the German Research Foundation (no. WO1712/3-1) to S.E.W., and an NSF grant (NSF BMAT; no. 1507736) to J.J.G. M.D.M. is a member of the Fonds de Recherche Quebec–Sante Network for Oral and Bone Health Research and the McGill Centre for Bone and Periodontal Research. **Author contributions:** D.A., W.J., and M.D.M. designed the overall experimental and analytical plan and drafted the initial manuscript. D.A. was involved in all experimental and analytical work. W.J. contributed to the AFM analysis. D.G., A.S., and R.R.C. contributed to the nanoindentation tests. H.V., K.B., and K.H.B. contributed to the TEM/tomography analyses. A.B.R.-N. contributed to the EBSD and 2D XRD data. M.T.H. provided the OPN extraction biochemical data. C.F.B. and S.E.W. prepared the wedge-polished sections. M.S.P. and J.J.G. performed the computational simulations. All authors analyzed and interpreted the data and participated in the writing and editing of the manuscript. M.D.M. provided overall supervision of the research. **Competing interests:** The authors declare that they have no competing interests. **Data and materials availability:** All data needed to evaluate the conclusions in the paper are present in the paper and/or the Supplementary Materials. Additional data related to this paper may be requested from the authors.

Submitted 25 October 2017
Accepted 13 February 2018
Published 30 March 2018
10.1126/sciadv.aar3219

Citation: D. Athanasiadou, W. Jiang, D. Goldbaum, A. Saleem, K. Basu, M. S. Pacella, C. F. Böhm, R. R. Chromik, M. T. Hincke, A. B. Rodríguez-Navarro, H. Vali, S. E. Wolf, J. J. Gray, K. H. Bui, M. D. McKee, Nanostructure, osteopontin, and mechanical properties of calcitic avian eggshell. *Sci. Adv.* **4**, eaar3219 (2018).